

# Spin-strain interaction in nitrogen-vacancy centers in diamond

Péter Udvarhelyi,<sup>1,2</sup> Vladyslav O. Shkolnikov,<sup>3</sup> Adam Gali,<sup>2,4</sup> Guido Burkard,<sup>3</sup> and András Pályi<sup>5,6</sup>

<sup>1</sup>Eötvös University, H-1117 Budapest, Hungary

<sup>2</sup>Wigner Research center for Physics, Hungarian Academy of Sciences, PO. Box 49, H-1525, Budapest, Hungary

<sup>3</sup>Department of Physics, University of Konstanz, D-78457 Konstanz, Germany

<sup>4</sup>Department of Atomic Physics, Budapest University of Technology and Economics, Budafoki út 8., H-1111 Budapest, Hungary

<sup>5</sup>Department of Physics, Budapest University of Technology and Economics, Budafoki út 8., H-1111 Budapest, Hungary

<sup>6</sup>MTA-BME Exotic Quantum Phases "Momentum" Research Group,

Budapest University of Technology and Economics, Budafoki út 8., H-1111 Budapest, Hungary

The interaction of solid-state electronic spins with deformations of their host crystal is an important ingredient in many experiments realizing quantum information processing schemes. Here, we theoretically characterize that interaction for a nitrogen-vacancy (NV) center in diamond. We derive the symmetry-allowed Hamiltonian describing the interaction between the ground-state spin-triplet electronic configuration and the local strain. We numerically calculate the six coupling-strength parameters of the Hamiltonian using density functional theory, and propose an experimental setup for measuring those coupling strengths. The importance of this interaction is highlighted by the fact that it enables to drive spin transitions, both magnetically allowed and forbidden, via mechanically or electrically driven spin resonance. This means that the ac magnetic field routinely used in a wide range of spin-resonance experiments with NV centers could in principle be replaced by ac strain or ac electric field, potentially offering lower power requirements, simplified device layouts, faster spin control, and local addressability of electronic spin qubits.

## I. INTRODUCTION

The nitrogen-vacancy (NV) color center consists of a nitrogen atom substituting a carbon atom adjacent to a vacancy in diamond (see Fig. 1). In the negatively charged state, it shows a broad fluorescence with zero-phonon-line at 637 nm<sup>1,2</sup> and possesses a spin  $S = 1$  ground state<sup>3-6</sup>. The electron spin of the NV center can be initialized, coherently manipulated, and read out in optically detected magnetic resonance (ODMR) experiments<sup>7</sup>, even at the level of individual centers<sup>8</sup>. This electronic spin degree of freedom is robust even at room temperature, and its coherence time is typically a few microseconds in natural diamond<sup>7</sup>, reaching milliseconds in <sup>12</sup>C enriched diamonds<sup>9</sup>. Because of these favorable properties of the NV center, it provides a versatile and highly coherent platform for the experimental realization of many quantum information schemes. To maximize the potential of these defects for various quantum communication<sup>10-12</sup>, quantum sensing<sup>13-21</sup>, and quantum computing<sup>22-24</sup> applications, it is crucial to understand the interaction of the center's electronic system with its environment, most notably externally induced electromagnetic fields, and deformations of the crystal lattice.

In this work, we provide a theoretical description of the latter, i.e., the *spin-strain interaction Hamiltonian* of the spin-triplet ground-state electronic configuration of the negatively charged NV defect. Even though in recent years this interaction has been studied intensively<sup>19-21,25-37</sup>, to our knowledge the correct and complete form of the interaction Hamiltonian of the ground-state spin-1 vector  $\mathbf{S}$  and the  $3 \times 3$  strain tensor  $\varepsilon$  has not been established in the literature. To fill this gap, we first derive the symmetry-allowed form of the spin-

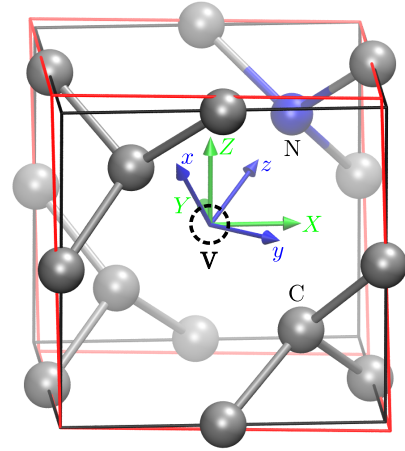


Figure 1. Nitrogen-vacancy (NV) center in the diamond lattice (Bravais cell depicted as a cube in black).  $\{X, Y, Z\}$  defines the cubic reference frame and  $\{x, y, z\}$  defines the NV reference frame. Deformation of the diamond crystal is visualized in red for  $\varepsilon_{xx} = 0.1$  strain component. We use this high strain only for sake of clarity.

strain interaction Hamiltonian, see Eq. (3). Second, we present numerical results for the six coupling-strength parameters appearing in the spin-strain interaction Hamiltonian (see Table I), which we compute using density functional theory (DFT); we find reasonable agreement with experimental results (see Table II). Third, we propose a setup to measure those two coupling-strength parameters which have not been experimentally characterized yet (Section V). Finally, we discuss how the spin-strain interaction can contribute to various applications of NVs in quantum information schemes (Section VI). In particular, our results reveal the possibility of using elec-

tric signals to control the magnetically allowed spin transitions of these defects, potentially offering lower power requirements, simplified device layouts, faster spin control, and local addressability of spin qubits.

We formulate our results in terms of the spin-stress interaction as well. We emphasize that our qualitative considerations apply more generally, to the whole family of spin-1 electronic states of defects with  $C_{3v}$  symmetry.

## II. PRELIMINARIES

We choose the *cubic reference frame* such that its origin coincides with the vacancy, and the nitrogen is at  $(a/4, a/4, a/4)$ , with  $a$  being the width of the cubic cell. The coordinates in the cubic frame are referred to as  $X, Y, Z$  (see Fig. 1). The *NV reference frame* is defined via its three orthonormal basis vectors,  $\mathbf{e}_z = (1, 1, 1)/\sqrt{3}$ ,  $\mathbf{e}_y = (1, -1, 0)/\sqrt{2}$ , and  $\mathbf{e}_x = \mathbf{e}_y \times \mathbf{e}_z$ . From now on, unless noted otherwise, we use the NV frame, and  $x, y$ , and  $z$  refers to coordinates in the NV frame. This choice of the reference frame implies that reflection upon the  $xz$  plane is a symmetry of the structure. This reflection, together with the 3-fold rotation around the  $z$  axis, generate the point group  $C_{3v}$  of the defect.

In the presence of a homogeneous magnetic field  $\mathbf{B} = (B_x, B_y, B_z)$ , and in the absence of any electric field and strain, the NV spin is described by the following Hamiltonian:

$$H_e/h = DS_z^2 + \gamma_e \mathbf{B} \cdot \mathbf{S}, \quad (1)$$

where  $h$  is Planck's constant,  $D = 2.87$  GHz is the zero-field splitting,  $\gamma_e = 2.8$  MHz/G is the electron gyromagnetic ratio, and  $\mathbf{S} = (S_x, S_y, S_z)$  is the vector of spin-1 Pauli matrices. The eigenstates and eigenvalues of  $S_z$  will be labelled according to  $S_z|m_S e\rangle = m_S|m_S e\rangle$ , where  $m_S \in \{-1, 0, +1\}$ .

The interaction Hamiltonian of a homogeneous electric field  $\mathbf{E} = (E_x, E_y, E_z)$  with the NV spin is constrained by the  $C_{3v}$  symmetry of the defect, and hence described by<sup>27,38,39</sup>

$$H_E = H_{E0} + H_{E1} + H_{E2}, \quad (2a)$$

$$H_{E0}/h = d_{\parallel} S_z^2 E_z, \quad (2b)$$

$$H_{E1}/h = d'_{\perp} [\{S_x, S_z\}E_x + \{S_y, S_z\}E_y], \quad (2c)$$

$$H_{E2}/h = d_{\perp} [(S_y^2 - S_x^2)E_x + \{S_x, S_y\}E_y]. \quad (2d)$$

Here, the lower indices 0, 1 and 2 refer to the difference in the electron spin quantum numbers ( $m_S$ ) connected by the corresponding Hamiltonian; e.g.,  $H_{E1}$  has nonzero matrix elements between  $|0e\rangle$  and  $|\pm 1e\rangle$ . The coefficients  $d_{\perp} = 17$  Hz cm/V and  $d_{\parallel} = 0.35$  Hz cm/V have been inferred in the experiment of Ref. 38. However, to our knowledge, the coefficient  $d'_{\perp}$  has not been quantified experimentally or theoretically; nevertheless it is expected<sup>27</sup> to have the same order of magnitude as  $d_{\perp}$ .

Two remarks on the spin-electric interaction Hamiltonian  $H_E$ : (1) The presence of  $H_{E1}$  in the spin-electric

Hamiltonian is a clear indication that coherent Rabi oscillations within the state pairs  $|0e\rangle \leftrightarrow | + 1e\rangle$  and  $|0e\rangle \leftrightarrow | - 1e\rangle$  can be driven by an ac electric field. This means, in principle, that any coherent-control experiment where these transitions are driven by ac magnetic field can also be done by replacing the ac magnetic field with an ac electric field, e.g., created by a single metallic gate electrode. To our knowledge, this opportunity which is routinely exploited for various solid-state spin systems<sup>40-43</sup> and is known as *electrically driven spin resonance* or *electric dipole spin resonance*, has been overlooked in the literature in the context of the magnetically allowed  $|0e\rangle \leftrightarrow | + 1e\rangle$  and  $|0e\rangle \leftrightarrow | - 1e\rangle$  transitions of NVs and similar defects with  $C_{3v}$  symmetry. Since electric control might bring significant advantages over magnetic control (simplified device layout, well-confined control fields allowing for local spin addressability, lower power requirements, etc), this observation provides a strong motivation to characterize the coupling-strength parameter  $d'_{\perp}$  of  $H_{E1}$  both experimentally and theoretically. (2) The experimental setup we propose in Sec. V to measure spin-stress and spin-strain coupling-strength parameters can be easily adopted to measure  $d'_{\perp}$ .

## III. SPIN-STRAIN HAMILTONIAN

In our understanding, the spin-strain interaction Hamiltonians used in the literature to characterize the NV (and similar defects with  $C_{3v}$  symmetry) are incomplete. A central result of the present work is the most general form of this Hamiltonian that is compatible with the  $C_{3v}$  symmetry of the NV. We find that this general symmetry-allowed Hamiltonian is characterized by six independent real *coupling-strength parameters*  $h_{41}, h_{43}, h_{25}, h_{26}, h_{15}, h_{16}$ , and has the following form:

$$H_{\varepsilon} = H_{\varepsilon 0} + H_{\varepsilon 1} + H_{\varepsilon 2}, \quad (3a)$$

$$H_{\varepsilon 0}/h = [h_{41}(\varepsilon_{xx} + \varepsilon_{yy}) + h_{43}\varepsilon_{zz}]S_z^2, \quad (3b)$$

$$H_{\varepsilon 1}/h = \frac{1}{2} \left[ h_{26}\varepsilon_{zx} - \frac{1}{2}h_{25}(\varepsilon_{xx} - \varepsilon_{yy}) \right] \{S_x, S_z\} + \frac{1}{2} (h_{26}\varepsilon_{yz} + h_{25}\varepsilon_{xy}) \{S_y, S_z\}, \quad (3c)$$

$$H_{\varepsilon 2}/h = \frac{1}{2} \left[ h_{16}\varepsilon_{zx} - \frac{1}{2}h_{15}(\varepsilon_{xx} - \varepsilon_{yy}) \right] (S_y^2 - S_x^2) + \frac{1}{2} (h_{16}\varepsilon_{yz} + h_{15}\varepsilon_{xy}) \{S_x, S_y\}, \quad (3d)$$

where  $\varepsilon_{ij} = (\partial u_i / \partial x_j + \partial u_j / \partial x_i) / 2$  denotes the strain tensor and  $\mathbf{u}(\mathbf{r})$  is the displacement field. Similarly to Eq. (2), the subscripts 0, 1, and 2 here refer to the difference in the electron spin quantum numbers  $m_S$  connected by the corresponding Hamiltonian. We present an elementary derivation of Eq. (3), as well as a derivation based on group representation theory, in Appendix A.

Note that the symmetry-allowed form of the spin-stress interaction, i.e., when the mechanical deformation is characterized by the  $3 \times 3$  stress tensor  $\sigma$  instead of

Table I. Spin-strain ( $h$ ) and spin-stress ( $g$ ) coupling-strength parameters calculated from density functional theory. See Appendix B for methodological details. Results are rounded to significant digits.

parameter	value (MHz/strain)	parameter	value (MHz/GPa)
$h_{43}$	$2300 \pm 200$	$g_{43}$	$2.4 \pm 0.2$
$h_{41}$	$-6420 \pm 90$	$g_{41}$	$-5.17 \pm 0.07$
$h_{25}$	$-2600 \pm 80$	$g_{25}$	$-2.17 \pm 0.07$
$h_{26}$	$-2830 \pm 70$	$g_{26}$	$-2.58 \pm 0.06$
$h_{15}$	$5700 \pm 200$	$g_{15}$	$3.6 \pm 0.1$
$h_{16}$	$19660 \pm 90$	$g_{16}$	$18.98 \pm 0.09$

strain  $\varepsilon$ , is completely analogous to Eq. (3). In what follows, we adopt a notation for the spin-stress Hamiltonian  $H_\sigma$  that is analogous to Eq. (3), with the substitutions  $\varepsilon \mapsto \sigma$  and  $h \mapsto g$ :

$$H_\sigma = H_{\sigma 0} + H_{\sigma 1} + H_{\sigma 2}, \quad (4a)$$

$$H_{\sigma 0}/h = [g_{41}(\sigma_{xx} + \sigma_{yy}) + g_{43}\sigma_{zz}] S_z^2, \quad (4b)$$

$$H_{\sigma 1}/h = \frac{1}{2} \left[ g_{26}\sigma_{xz} - \frac{1}{2}g_{25}(\sigma_{xx} - \sigma_{yy}) \right] \{S_x, S_z\} + \frac{1}{2}(g_{26}\sigma_{yz} + g_{25}\sigma_{xy})\{S_y, S_z\}, \quad (4c)$$

$$H_{\sigma 2}/h = \frac{1}{2} \left[ g_{16}\sigma_{xz} - \frac{1}{2}g_{15}(\sigma_{xx} - \sigma_{yy}) \right] (S_y^2 - S_x^2) + \frac{1}{2}(g_{16}\sigma_{yz} + g_{15}\sigma_{xy})\{S_x, S_y\}. \quad (4d)$$

Many recent works (e.g., Refs. 19, 21, and 31) rely on a heuristic spin-strain Hamiltonians built on an unjustified analogy between strain and electric field. That approach does not take into account the  $3 \times 3$  tensor structure of strain, therefore it provides an incorrect description of the spin-strain interaction, even in the absence shear strain. A recent work<sup>34</sup> uses a spin-stress Hamiltonian based on the  $3 \times 3$  stress tensor  $\sigma$ ; their Hamiltonian includes 4 real parameters,  $a_1$ ,  $a_2$ ,  $b$  and  $c$ . That Hamiltonian is equivalent to our  $H_{\sigma 0} + H_{\sigma 2}$ ; but incomplete as it lacks the symmetry-allowed term  $H_{\sigma 1}$  analogous to Eq. (3c); we provide more details on its relation to our results in Sec. IV. We note that using the incomplete  $H_{\sigma 0} + H_{\sigma 2}$  Hamiltonian in Ref. 34 is justified as an approximation, since the term  $H_{\sigma 1}$  is a small perturbation in the magnetic-field range addressed in those experiments. We also remark that in a very recent work<sup>44</sup>, a spin-phonon interaction Hamiltonian incorporating matrix elements between  $|0e\rangle$  and  $|\pm 1e\rangle$  has been used to describe spin relaxation in NVs.

#### IV. SPIN-STRAIN PARAMETERS FROM DENSITY FUNCTIONAL THEORY

We use DFT to numerically compute the six coupling-strength coefficients  $h_{41}$ , etc., appearing in the spin-strain Hamiltonian (3). Methodological details are presented in Appendix B. The results are summarized in Table I. Therein, we also present the spin-stress coupling-strength coefficients  $g_{41}$ , etc, which we obtain from the  $h$  values using the stiffness tensor of bulk diamond, see Appendix C.

In Table II, we compare the numerical DFT results of Table I to the experimental results of Ref. 34. In Ref. 34, four out of the six independent spin-stress coupling-strength parameters of the spin-stress interaction Hamiltonian were measured. Ref. 34 defines these 4 spin-stress coupling-strength parameters, denoted as  $a_1$ ,  $a_2$ ,  $b$ ,  $c$ , in a ‘hybrid’ representation, where the spin-stress Hamiltonian is expressed in terms of the NV-frame components of the spin vector ( $S_x$ ,  $S_y$ ,  $S_z$ ) and the cubic-frame components of the stress tensor ( $\sigma_{XX}$ ,  $\sigma_{XY}$ , etc). To be able to make a comparison between our DFT results and the experimental ones, we now take the notations of Ref. 34, and introduce  $d$ ,  $e$ ,  $\mathcal{N}_x$ ,  $\mathcal{N}_y$ , to express our spin-stress Hamiltonian  $H_\sigma$  in Eq. (4) in this hybrid representation:

$$H_{\sigma 0}/h = \mathcal{M}_z S_z^2, \quad (5a)$$

$$H_{\sigma 1}/h = \mathcal{N}_x \{S_x, S_z\} + \mathcal{N}_y \{S_y, S_z\}, \quad (5b)$$

$$H_{\sigma 2}/h = -\mathcal{M}_x (S_x^2 - S_y^2) + \mathcal{M}_y \{S_x, S_y\}, \quad (5c)$$

where

$$\mathcal{M}_z = a_1(\sigma_{XX} + \sigma_{YY} + \sigma_{ZZ}) + 2a_2(\sigma_{YZ} + \sigma_{ZX} + \sigma_{XY}), \quad (6a)$$

$$\mathcal{N}_x = d(2\sigma_{ZZ} - \sigma_{XX} - \sigma_{YY}) + e(2\sigma_{XY} - \sigma_{YZ} - \sigma_{ZX}), \quad (6b)$$

$$\mathcal{N}_y = \sqrt{3} [d(\sigma_{XX} - \sigma_{YY}) + e(\sigma_{YZ} - \sigma_{ZX})], \quad (6c)$$

$$\mathcal{M}_x = b(2\sigma_{ZZ} - \sigma_{XX} - \sigma_{YY}) + c(2\sigma_{XY} - \sigma_{YZ} - \sigma_{ZX}), \quad (6d)$$

$$\mathcal{M}_y = \sqrt{3} [b(\sigma_{XX} - \sigma_{YY}) + c(\sigma_{YZ} - \sigma_{ZX})]. \quad (6e)$$

The relations between the hybrid-representation parameters ( $a_1$ ,  $a_2$ ,  $b$ ,  $c$ ,  $d$ ,  $e$ ) and the NV-frame parameters ( $g_{41}$ , etc) are given in the first two columns of Table II. Importantly,  $H_{\sigma 0}$  and  $H_{\sigma 2}$  is identical to the spin-stress Hamiltonian in Eqs. (1) and (2) of Ref. 34.

In Table II, the DFT results for the cubic-frame spin-strain coupling-strength parameters are listed in the third column, whereas the experimental values<sup>34</sup> are listed in the fourth column.<sup>45</sup> According to Table II, the signs of the DFT and experimental results are the same, and for all 4 parameters determined from the experiment, the order of magnitude matches well with that of the DFT result. This suggests that the DFT method applied here captures the key mechanism of interaction between the electron spin and the mechanical deformation, and gives

Table II. Spin-stress coupling-strength parameters: Comparison of density functional theory and experimental<sup>34</sup> results. Parameters in the hybrid representation ( $a_1$ ,  $a_2$ , etc.) are expressed in terms of the parameters in the NV-frame representation ( $g_{41}$ , etc) in the second column. Par. and exp. are abbreviations for ‘parameters’ and ‘experimental results’.

par.	relation	DFT (MHz/GPa)	exp. <sup>34</sup> (MHz/GPa)
$a_1$	$\frac{2g_{41}+g_{43}}{3}$	$-2.66 \pm 0.07$	$-4.4 \pm 0.2$
$a_2$	$\frac{-g_{41}+g_{43}}{3}$	$2.51 \pm 0.06$	$3.7 \pm 0.2$
$b$	$\frac{-g_{15}+\sqrt{2}g_{16}}{12}$	$1.94 \pm 0.02$	$2.3 \pm 0.3$
$c$	$\frac{-2g_{15}-\sqrt{2}g_{16}}{12}$	$-2.83 \pm 0.03$	$-3.5 \pm 0.3$
$d$	$\frac{-g_{25}+\sqrt{2}g_{26}}{12}$	$-0.12 \pm 0.01$	-
$e$	$\frac{-2g_{25}-\sqrt{2}g_{26}}{12}$	$0.66 \pm 0.01$	-

confidence in the predictions for the previously omitted parameters  $d$  and  $e$ .

## V. METHODS TO MEASURE THE SPIN-STRESS PARAMETERS

To our knowledge, the spin-stress coupling strength parameters  $g_{25}$  and  $g_{26}$  have not yet been measured. In this section, we propose a method that allows to determine those in an experiment which combines the controlled application of mechanical stress and ODMR. The method, inspired by the experiment of Ref. 46, requires a finite magnetic field along the NV axis, which tunes the system to the ground-state level anticrossing (GSLAC) where the  $|-1e\rangle$  and  $|0e\rangle$  electronic states are approximately degenerate,  $B_z \approx B_g \equiv D/\gamma_e \approx 1024$  G. In that setting, mechanical stress can induce strong mixing of the spin eigenstates of the coupled electron-nuclear system via the coupling-strength parameters  $g_{25}$  and  $g_{26}$ . In turn, the spin dynamics governed by this mixing can be detected in a time-resolved fashion, via photoluminescence-based optical readout of the NV spin system. First, in Section V A, we introduce our model, and show that the mechanical stress can be thought of as an extra contribution to the external magnetic field, see Eq. (12). Second, in Section V B, we describe an arrangement that can be used to determine the axial spin-stress coupling-strength parameters  $g_{41}$  and  $g_{43}$ . Third, in Section V C, we outline the experiment to determine the transverse coupling-strength parameters  $g_{25}$  and  $g_{26}$ .

### A. Effective magnetic field due to mechanical stress

The measurement schemes described here work in the vicinity of the GSLAC, where the  $|-1e\rangle$  and  $|0e\rangle$  electronic spin levels are nearly degenerate. This is where the stress-induced terms of  $H_{\sigma 1}$ , which are typically much smaller than the zero-field spin splitting  $D$ , are most effective in mixing these two electronic spin states. Due to

the presence of the N nuclear spin and hyperfine interaction, there is a hyperfine structure of the energy spectrum at the GSLAC<sup>47</sup>. This is illustrated for the case of an  $^{14}\text{N}$  nuclear spin in Fig. 2: instead of two electron spin levels crossing at  $B_z = B_g$ , there are six levels, with two level pairs showing hyperfine-induced anticrossings. We focus on the case when the N atom of the NV center is an  $^{14}\text{N}$ ; the analysis can be generalized straightforwardly for the  $^{15}\text{N}$  case<sup>46,48</sup>.

We assume that a magnetic field  $B_z \approx B_g$  is applied, aligned with the NV axis. Formally we write the magnetic field vector as  $\mathbf{B} = (B_x, B_y, B_z)$ , but we will consider only the case  $B_x = B_y = 0$ . The 9-dimensional Hamiltonian describing the coupled electron-nuclear system in the presence of the magnetic field and mechanical stress reads

$$H = H_e + H_\sigma + H_n + H_{hf}, \quad (7)$$

where  $H_e$  is defined in Eq. (1),  $H_\sigma$  is defined in Eq. (4),  $H_n$  describes the nuclear Zeeman effect and the quadrupole moment of the  $I = 1$  spin of the  $^{14}\text{N}$  via

$$H_n/h = -\gamma_n B_z I_z + Q I_z^2, \quad (8)$$

and  $H_{hf}$  describes the hyperfine interaction via

$$H_{hf}/h = A_{||} S_z I_z + A_{\perp} (S_x I_x + S_y I_y). \quad (9)$$

We use the eigenstates of  $I_z$  as the basis for the nuclear spin states, labelled according to  $I_z|m_I n\rangle = m_I|m_I n\rangle$ , where  $m_I \in \{-1, 0, +1\}$ . Note that in  $H_n$  we use  $\mathbf{B} = (0, 0, B_g)$  for simplicity. The literature values of the coefficients<sup>49</sup> are  $Q = -5.01$  MHz,  $A_{||} = -2.14$  MHz,  $A_{\perp} = -2.7$  MHz.

The six low-energy eigenstates of the 9x9 Hamiltonian  $H$  are shown in Fig. 2 as a function of the axial magnetic field  $B_z$ , in the vicinity of the GSLAC. For this plot, zero stress is assumed. Solid lines highlight the three levels that will be utilized to determine the spin-stress coupling-strength parameters. In Fig. 2, anticrossings are induced by hyperfine interaction, but far from the anticrossings the depicted energy eigenstates are eigenstates of  $S_z$  and  $I_z$  to a good approximation, and therefore are labelled accordingly, as  $|m_S e, m_I n\rangle$ .

When describing the effect of a nonzero mechanical stress, it is possible and helpful to introduce the notion of an *effective magnetic field* vector  $(\Phi_x, \Phi_y, \Phi_z)$ , which describes the combined effect of the actual magnetic field and the stress-induced terms in the Hamiltonian. To see this, let us first focus on the electronic degree of freedom and the 2-dimensional low-energy electron spin subspace at the GSLAC. The electronic Hamiltonian in this 2-dimensional subspace is expressed using the corresponding projector  $P = |0e\rangle\langle 0e| + |-1e\rangle\langle -1e|$  as

$$P H_e P = h\gamma_e \begin{pmatrix} 0 & \frac{B_x - iB_y}{\sqrt{2}} \\ \frac{B_x + iB_y}{\sqrt{2}} & B_g - B_z \end{pmatrix}. \quad (10)$$

In the presence of a nonzero stress, described by the matrix  $\sigma$ , this Hamiltonian generalizes to

$$P(H_e + H_\sigma)P = h\gamma_e \begin{pmatrix} 0 & \frac{\Phi_x - i\Phi_y}{\sqrt{2}} \\ \frac{\Phi_x + i\Phi_y}{\sqrt{2}} & B_g - \Phi_z \end{pmatrix}, \quad (11)$$

where we introduced the effective magnetic field components

$$\Phi_x = B_x + \frac{g_{25}}{4\gamma_e}(\sigma_{xx} - \sigma_{yy}) - \frac{g_{26}}{2\gamma_e}\sigma_{xz}, \quad (12a)$$

$$\Phi_y = B_y - \frac{g_{25}}{2\gamma_e}\sigma_{xy} - \frac{g_{26}}{2\gamma_e}\sigma_{yz}, \quad (12b)$$

$$\Phi_z = B_z - \frac{g_{41}}{\gamma_e}(\sigma_{xx} + \sigma_{yy}) - \frac{g_{43}}{\gamma_e}\sigma_{zz}. \quad (12c)$$

These expressions reveal that the mechanical stress can be thought of as an extra contribution to the applied magnetic field.

### B. Measuring the axial spin-stress parameters $g_{41}$ ,

$g_{43}$

Our proposed experiment to determine  $g_{41}$  and  $g_{43}$  combines a controlled application of static uniaxial stress, and optically detected magnetic resonance<sup>46</sup>, in an axial magnetic field that tunes the NV spin system to the GSLAC. Note that these coupling-strength parameters have already been experimentally characterized by a different method in Ref. 34.

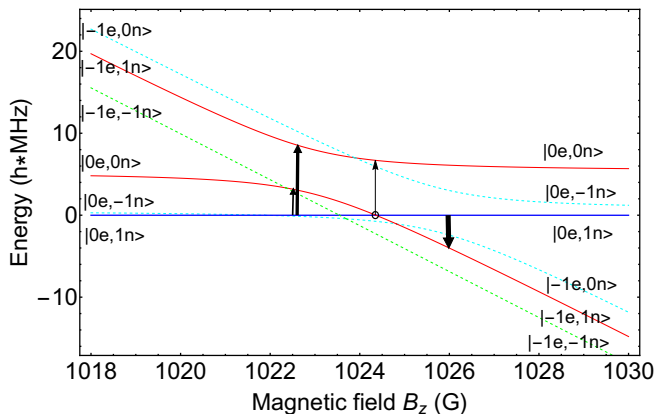


Figure 2. Level structure of the  $^{14}\text{NV}$  at the GSLAC as a function of the axial magnetic field  $B_z$ . All transverse magnetic field components and stress are zero,  $B_x = B_y = 0$ ,  $\sigma = 0$ . The circle marks the crossing that serves to identify the stress coupling coefficients  $g_{25}$ ,  $g_{26}$ . The levels coupled by the hyperfine interaction are shown with the same color (red solid; light blue dashed). The arrows indicate the bright radiofrequency magnetic transitions at the corresponding values of the magnetic field. In the absence of mechanical stress, the dashed lines are invisible in optically detected magnetic resonance.

The first stage of our proposed experiment is the observation of certain parts of the hyperfine level structure shown in Fig. 2. At this stage, no mechanical stress is applied. In the vicinity of the GSLAC, at  $(B_x, B_y, B_z) \approx (0, 0, B_g)$ , the coupled electron-nuclear spin system is initialized to the state  $|\psi(0)\rangle = |0e, -1n\rangle$  (blue solid line in Fig. 2) with an optical pulse. Then, an ac magnetic pulse of a given frequency  $f$ , amplitude  $B_{ac}$ , and duration  $\tau$  is applied. On the one hand, if that magnetic pulse is off-resonant with respect to all energy eigenstates in Fig. 2, then the spin system remains in its initial state,  $|\psi(\tau)\rangle \propto |0e, -1n\rangle$ . Then, a readout optical pulse at time  $t = \tau$  will result in significant photoluminescence which is measured. Note that the photoluminescence after the readout pulse is proportional to the occupation probability of the  $|0e\rangle$  electron spin state, i.e., to the quantity  $\sum_{m_I} |\langle 0e, m_I n | \psi(\tau) \rangle|^2$ . On the other hand, if the magnetic field pulse is resonant with one of the transitions in Fig. 2, then it can change the initial state to a state  $|\psi(\tau)\rangle$  that contains a reduced weight of the  $|0e\rangle$  state, and thereby the photoluminescence signal decreases.

To quantify this drop in the photoluminescence signal upon resonant excitation, we will use the quantity

$$C = 1 - \sum_{m_I=-1,0,1} |\langle 0e, m_I n | \psi(\tau) \rangle|^2, \quad (13)$$

and call it the *photoluminescence contrast*. This quantity characterizes how effective the magnetic pulse is in inducing spin transitions: the value of  $C$  is zero for an off-resonant magnetic pulse, and can take values between 0 and 1 for a resonant magnetic pulse.

The black curves in Fig. 3b visualize the predicted outcome of this experiment using the photoluminescence contrast  $C$ , cf. Fig. 2 of Ref. 46. Our Fig. 3b demonstrates that key features of the hyperfine structure of the spin levels of Fig. 2 can be mapped using this experimental technique. To generate this plot, we calculated the five resonant transition frequencies from the spectral gaps in Fig. 2. We plot these five curves in Fig. 3b, where the thickness of each curve is rescaled by the corresponding photoluminescence contrast  $C$ . Hence, the black curves in Fig. 3b reveal that for a given magnetic field, at most two out of the five transitions are bright. The bright transitions at three specific  $B_z$  values are also indicated in Fig. 2. We calculated the photoluminescence contrast  $C$  based on standard two-level Rabi dynamics in the rotating wave approximation, assuming resonant driving frequency  $f$ , a magnetic pulse strength  $b = g\mu_B B_{ac}\tau/h = \sqrt{2}/4$ , and the ac magnetic field vector being aligned with the  $x$  axis. Note that the above pulse strength  $b$  corresponds to an exact electron-spin  $\pi$ -pulse away from the GSLAC.

The second stage of the experiment is to repeat this ODMR spectroscopy in the presence of uniaxial  $z$ -directional strain,  $\sigma_{zz} \neq 0$ . The predicted photoluminescence contrast for the case of  $\sigma_{zz} = 1 \text{ GPa}$  is shown by the orange curves in Fig. 3b. Apparently, the spectrum

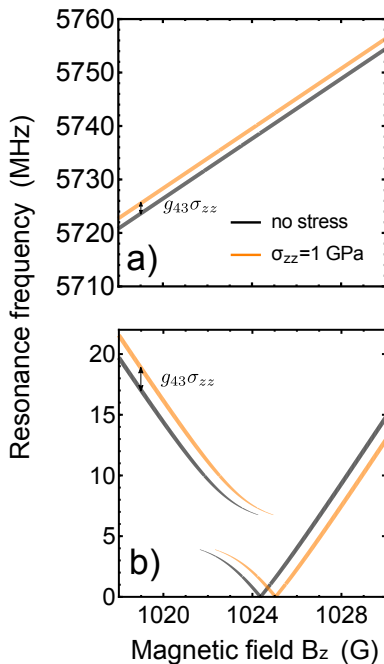


Figure 3. Effect of mechanical stress on the photoluminescence contrast in optically detected magnetic resonance of an  $^{14}\text{NV}$  centre. Black: no stress, orange:  $\sigma_{zz} = 1$  GPa. The curves show the dependence of hyperfine transition frequencies as function of the axial magnetic field  $B_z$  in the vicinity of the GSLAC. The thickness of each curve is proportional to the photoluminescence contrast  $C$  (Eq. 13); maximal thickness corresponds to  $C = 1$ . (a) High-energy transitions to  $|1e\rangle$  spin states. (b) Low-energy transitions within the subspace of  $|0e\rangle$  and  $|-1e\rangle$ .

shifts along the  $B_z$  axis. Measuring this shift reveals the spin-stress coupling-strength parameter  $g_{43}$ . In fact, simple analytical expressions can be obtained for the locations of the ODMR resonances, including the effect of the considered uniaxial strain. By projecting the  $9 \times 9$  Hamiltonian  $H$  to the two-dimensional subspace of  $|0e, 0n\rangle$  and  $|-1e, 1n\rangle$ , and diagonalizing the resulting  $2 \times 2$  Hamiltonian, we obtain the resonance frequencies corresponding to the bright low-frequency transitions (blue  $\rightarrow$  red transitions in Fig. 2):

$$f_{\pm} = \left| \frac{1}{2} \left( -A_{\parallel} + D \left( 1 + \frac{\gamma_n}{\gamma_e} \right) - Q - \gamma_e \Phi_z \right) \pm \sqrt{A_{\perp}^2 + \frac{1}{4} \left( A_{\parallel} - D \left( 1 - \frac{\gamma_n}{\gamma_e} \right) - Q + \gamma_e \Phi_z \right)^2} \right|, \quad (14)$$

For magnetic fields significantly below the GSLAC, e.g., around  $B_z = 1019$  G in Fig. 3b, the bright transition resonance frequency can be approximated by making a zeroth-order expansion of  $f_{+}$  (see Eq. (14)) in  $A_{\perp}$ , and substituting Eq. (12c) to the result, yielding

$$f_{+} \approx -A_{\parallel} + D - \gamma_e B_z + g_{43} \sigma_{zz}. \quad (15)$$

This implies that  $g_{43}$  can be directly calculated from the measured stress-induced shift of the resonance frequency

at a given magnetic field (e.g.,  $B_z = 1019$  G) via

$$g_{43} = \frac{f_{+}(B_z, \sigma_{zz}) - f_{+}(B_z, 0)}{\sigma_{zz}}. \quad (16)$$

The third, last stage of the experiment is to obtain  $g_{41}$  by repeating this ODMR spectroscopy in the presence of uniaxial stress along  $\mathbf{n} = (1, 1, 0)/\sqrt{2}$ . In that case, the stress tensor reads  $\sigma_{ij} = n_i n_j \sigma$ , hence the three components  $\sigma_{xx} = \sigma_{yy} = \sigma_{xy} = \sigma/2$  are nonzero. Because of the nonzero off-diagonal component  $\sigma_{xy}$ , a nonzero effective magnetic field component  $\Phi_y$  is present, see Eq. (12b), seemingly complicating the previous analysis. However, assuming that our DFT predictions in Table I for the coupling-strength orders of magnitude are correct, the effect of this  $\sigma_{xy}$ -induced effective transverse magnetic field component on the energy spectrum can be neglected away from the anticrossing, e.g., at  $B_z = 1019$  G. Therefore, in this situation the stress-induced shift of the resonance frequency can be translated to the coupling-strength parameter  $g_{41}$  via

$$g_{41} = \frac{f_{+}(B_z, \sigma) - f_{+}(B_z, 0)}{\sigma}. \quad (17)$$

We note that these coupling-strength coefficients  $g_{41}$  and  $g_{43}$  can also be determined by utilizing the high-energy  $|1e, 1n\rangle$  spin state at the GSLAC and the corresponding  $\sim 6$  GHz ac magnetic field pulses. This is illustrated by Fig. 3a, where the photoluminescence contrast corresponding to the  $|0e, 1n\rangle \rightarrow |1e, 1n\rangle$  transition is shown in the absence (black) and presence (orange) of z-directional mechanical stress. The relation between the coupling-strength parameters and the shift of the resonance frequency is the same as for the low-energy transitions, see Eqs. (16) and (17).

### C. Measuring the transverse spin-stress parameters $g_{25}, g_{26}$

Here we propose and quantitatively analyze a method for measuring the transverse spin-stress coupling-strength coefficients  $g_{25}, g_{26}$ . Similarly to the method in the preceding subsection, this method also works in the vicinity of the GSLAC. It is based on the experiment discussed and implemented in Section IV of Ref. 46, where Larmor-precession spin dynamics was used to precisely measure the magnetic-field component perpendicular to the NV axis (see, e.g., their Fig. 3). Here we focus on how to measure the coupling strengths  $g_{25}, g_{26}$  in the case when the magnetic field is aligned with the NV axis. Our method relies on the observation of Larmor-precession spin dynamics, which is affected by stress via the spin-stress interaction described by Eq. (4). The role of the transverse magnetic field components  $B_x$  and  $B_y$  in the experiment of Ref. 46 is played by the stress-induced transverse effective magnetic field components  $\Phi_x$  and  $\Phi_y$  in our setup.

First, recall the experimental scheme of Ref. 46 for the special case when  $B_z$  is tuned to the blue-red level crossing in Fig. 2,  $B_z = B_c$ , denoted by a circle. The two states that meet at the crossing are, to a good approximation,  $|0e, 1n\rangle$  and  $|\chi\rangle = \frac{1}{\sqrt{1+\alpha^2}}(\alpha|0e, 0n\rangle + |-1e, 1n\rangle)$ , where  $\alpha = \frac{\gamma_e A_\perp}{Q\gamma_e - D\gamma_n} \approx 0.5$ . For the readout, it will prove important that the weight of  $|\chi\rangle$  in the  $|0e\rangle$  subspace is  $|\langle 0e, 0n|\chi\rangle|^2 \approx 0.2$ , significantly lower than 1. In the presence of a small transverse magnetic field, the blue-red level crossing in Fig. 2 is split to an anticrossing, due to a coupling Hamiltonian matrix element between these states, which enters the two-level Hamiltonian of  $|0e, 1n\rangle$  and  $|\chi\rangle$  as

$$H_L = \frac{h\gamma_e}{\sqrt{2(1+\alpha^2)}} \begin{pmatrix} 0 & B_x - iB_y \\ B_x + iB_y & 0 \end{pmatrix}. \quad (18)$$

In this setup, the experiment starts with an optical pulse that initializes the spin system in  $|\psi(0)\rangle = |0e, 1n\rangle$  at  $t = 0$ . Because of the finite transverse magnetic field in Eq. (18), this initial state is not an energy eigenstate, and therefore the time evolution  $|\psi(t)\rangle$  exhibits complete Larmor-precession cycles between the two states  $|0e, 1n\rangle$  and  $|\chi\rangle$ . To observe this Larmor precession, the photoluminescence contrast  $C(\tau)$  was measured<sup>46</sup> as a function of the waiting time  $\tau$  following the initialization. This photoluminescence contrast  $C(\tau)$  reveals the Larmor precession, since the state  $|\chi\rangle$  is mostly outside the  $|0e\rangle$  subspace. The frequency of this Larmor precession is derived from Eq. (18):

$$f_L = \sqrt{\frac{2}{1+\alpha^2}} \gamma_e \sqrt{B_x^2 + B_y^2}. \quad (19)$$

Here, we suggest to adopt this scheme to characterize the effective transverse magnetic field components  $\Phi_x$  and  $\Phi_y$  defined in Eq. (12), and thereby measure the spin-stress coupling-strength coefficients  $g_{25}$  and  $g_{26}$ . For simplicity, we make the following specifications. First, we take  $B_x = B_y = 0$ . Second, for an arbitrary uniaxial stress  $\sigma_{ij} = \sigma n_i n_j$ , defined by its direction  $\mathbf{n} = (n_x, n_y, n_z)$  and magnitude  $\sigma$ , we suggest to tune  $B_z$  to the ‘virtual crossing point’, i.e., to a value  $B_z = \tilde{B}_c$ , where the energy eigenvalues of  $|0e, 1n\rangle$  and  $|\chi\rangle$  would be degenerate in the virtual situation when the transverse effective magnetic field components are turned off,  $\Phi_x = \Phi_y = 0$ . That is guaranteed for  $\Phi_z = B_c$ , which, together with Eq. (12c) implies

$$\tilde{B}_c = B_c + \frac{g_{41}(n_x^2 + n_y^2) + g_{43}n_z^2}{\gamma_e}. \quad (20)$$

This simple expression reveals that this virtual crossing point can be identified once the parameters  $g_{41}$  and  $g_{43}$  have been measured, e.g., using the method of the preceding section.

At this virtual crossing point, the role of the transverse effective magnetic fields  $\Phi_x$  and  $\Phi_y$  is completely analogous to the role of  $B_x$  and  $B_y$  in Ref. 46. Namely,

they force the spin system initialized in  $|0e, 1n\rangle$  to exhibit complete Larmor precessions between the states  $|0e, 1n\rangle$  and  $|\chi\rangle$ , with the Larmor frequency (cf. Eq. (19))

$$f_L = \sqrt{\frac{2}{1+\alpha^2}} \gamma_e \sqrt{\Phi_x^2 + \Phi_y^2}. \quad (21)$$

From this, and using Eq. (12) for the effective magnetic fields, we find

$$f_L = \sqrt{\frac{\frac{g_{25}^2}{4} n_\perp^4 + g_{26}^2 n_z^2 n_\perp^2 + g_{25} g_{26} n_x n_z (3n_y^2 - n_z^2)}{2(1+\alpha^2)}} |\sigma|, \quad (22)$$

with  $n_\perp = \sqrt{n_x^2 + n_y^2}$ .

Our result (22) allows the identification of the coefficients  $g_{25}$  and  $g_{26}$  by applying the uniaxial stress in different directions and then measuring the Larmor precession frequency. For example, the absolute value of  $g_{25}$  can independently be measured by applying the uniaxial stress in the direction  $\mathbf{n} = (1, 1, 0)/\sqrt{2}$ . In that case, Eq. (22) implies that this coupling-strength parameter is deduced from the measured Larmor frequency via

$$|g_{25}| = \sqrt{8(1+\alpha^2)} \frac{f_L}{|\sigma|} \approx 3.17 \frac{f_L}{|\sigma|}. \quad (23)$$

Analogously, the absolute value of  $g_{26}$  can independently be measured with the uniaxial stress applied in the direction  $\mathbf{n} = (\sqrt{3}, 1, 1)/\sqrt{5}$ ; for that case, we find

$$|g_{26}| = \frac{\sqrt{10(1+\alpha^2)}}{2} \frac{f_L}{|\sigma|} \approx 1.77 \frac{f_L}{|\sigma|}. \quad (24)$$

We note that this procedure only allows us to determine the absolute values of the coupling-strength coefficients. Nevertheless, it is straightforward to generalize the above procedure to determine the signs of the coefficients by utilizing a finite transverse magnetic field. E.g., following up on our first example above, let us assume that we apply compressive uniaxial strain  $\sigma < 0$  along  $\mathbf{n} = (1, 1, 0)/\sqrt{2}$ . If the sign of  $g_{25}$  is indeed negative, as indicated by our DFT results in Table I, then the transverse effective magnetic field components read  $\Phi_x = 0$  and  $\Phi_y = B_y - p|\sigma|$ , with  $p > 0$ . Hence, according to Eq. (22), the Larmor precession is slowed down gradually as a magnetic field component along the y axis is switched on. On the other hand, if the sign of  $g_{25}$  is positive, then a small y-directional magnetic field will speed up the Larmor precession.

## VI. DISCUSSION

### A. Potential applications

*Time-dependent mechanical deformation for resonant spin control.* Coherent spin control in NVs via ac mechanical deformation has been demonstrated with  $\sim 1$

MHz Rabi frequency for the magnetically forbidden  $| -1e \rangle \leftrightarrow | 1e \rangle$  transition<sup>20</sup>. Our results imply that the other two, magnetically allowed, transitions,  $| 0e \rangle \leftrightarrow | \pm 1e \rangle$ , can also be induced in a similar fashion. This suggests that, in principle, the ac magnetic field used routinely for spin control in NV-based experiments can be substituted by ac mechanical driving. From the spin-strain Hamiltonian  $H_\varepsilon$  of Eq. (3), we estimate that an ac strain  $\varepsilon_{xx}$  with an amplitude of 0.01 can provide mechanically induced Rabi oscillations for the magnetically allowed transitions with a Rabi frequency of  $\sim 5$  MHz.

*Time-dependent electric fields for resonant spin control.* According to Eq. (2), an externally induced electric field interacts with the NV spin, allowing for coherent electric control of all three spin transitions of the NV. Electric control of the magnetically forbidden transition has been demonstrated in SiC<sup>43</sup>, but that of the magnetically allowed transitions has yet to be achieved. In Ref. 43, electrical Rabi frequencies of  $\sim 1$  MHz were realized for the magnetically forbidden transition. This Rabi frequency is proportional to the coupling-strength parameter  $d_\perp$ . Furthermore, from the dielectric strength of SiC it was estimated that  $\sim 60$  MHz electrical Rabi frequencies should be reachable, comparable to magnetic spin control with millitesla driving strength<sup>50,51</sup>. Noting that the  $d_\perp$  parameter and the dielectric strength are similar for NV centers in diamond, and the  $d'_\perp$  parameter is expected<sup>27</sup> to be of the same order of magnitude as  $d_\perp$ , we speculate that the electrical Rabi frequencies for the magnetically allowed transitions in diamond NVs centers could also reach a few tens of MHz.

*Electrically driven, mechanically assisted spin resonance using piezoelectric elements.* Our results regarding the spin-strain coupling in  $C_{3v}$  symmetric defects promote a new way of using electric signals for coherent control, for all three transitions between the spin-1 basis states. Dynamical mechanical deformation can be created by ac electric fields (voltages) via piezoelectric elements attached to the diamond crystal, e.g., a ZnO layer. The functionality of such arrangements has already been experimentally demonstrated using interdigital transducers serving as transmitters and receivers of surface acoustic waves of the diamond crystal<sup>35,36</sup>. The magnitude of strain created by the ac electric field could further be enhanced using mechanical cavity resonators<sup>52</sup> for the surface acoustic waves. The mechanical waves, when tuned to resonance with the defect spin transition frequency, can then drive coherent spin Rabi oscillations. This working principle allows for devices where coherent control of the defect spins is performed via electrically driven, mechanically assisted spin resonance.

## B. Open problems

*Experimental characterization of the spin-strain and the spin-electric parameters.* As discussed above, the spin-strain (spin-stress) coupling-strength parameters of

$H_{\varepsilon 1}$  ( $H_{\sigma 1}$ ), namely  $h_{25}$  and  $h_{26}$  ( $g_{25}$  and  $g_{26}$ , or  $d$  and  $e$ , depending on the representation), are yet to be characterized experimentally. Similarly, the corresponding spin-electric coupling-strength coefficient<sup>27</sup>  $d'_\perp$  in Eq. (2) is yet to be measured. We emphasize the technological relevance of these parameters: the terms they multiply in the Hamiltonian can induce magnetically allowed spin transitions, i.e., of the  $| 0e \rangle \leftrightarrow | \pm 1e \rangle$  type; therefore, for systems where these parameters are sufficiently strong, ac electric or ac mechanical driving could substitute the ac magnetic field that is routinely used in most coherent spin-control experiments.

*Quantitative description of mechanically and electrically driven electron spin resonance.* The static spin-strain Hamiltonian (3) and the DFT-based coupling-strength parameters in Table I can be used to estimate the time scale (Rabi time) of spin control for an ac mechanical drive with a given strain pattern. However, it is known from the theory of spin-orbit-mediated electrically driven spin resonance<sup>42,53</sup>, that even if an electric field does not modify the spin Zeeman splitting, it can induce transition between spin states. Hence it is expected that an accurate description of mechanically or electrically driven spin resonance for the NV, which probably involves electronic spin-spin and spin-orbit interactions, requires a careful treatment of dynamical effects.

*Interaction of strain and electric fields with nuclear spins.* The coherence time of the nuclear spin of the N atom in the NV exceeds that of the ground-state electronic spin, and can be used as a long-lived quantum memory<sup>54</sup>. Furthermore, the NV can interact with <sup>13</sup>C nuclear spins located in its vicinity. These highly coherent nuclear spins are heavily exploited in NV-based quantum-control experiments<sup>22-24,46,55,56</sup>, which is a strong motivation to understand the interaction of solid-state nuclear spins with electric and strain fields. Important steps in this direction have already been taken<sup>57-62</sup>, but the experimental and theoretical characterization of the spin-electric and spin-strain interactions for NV nuclear spins is yet to be done.

We anticipate that the nature of the problem is qualitatively different for (i) a spin-1/2 nuclear spin, e.g., of a <sup>15</sup>N or a <sup>13</sup>C atom, and (ii) a nuclear spin that is larger than 1/2, e.g., of a <sup>14</sup>N atom. In case (i) the nuclear spin does not interact directly with electric or strain fields<sup>63</sup>. However, these fields do interact with the electronic spin, which can serve as a quantum transducer that translates these fields to the nucleus via the hyperfine interaction<sup>55,58,59,61,64,65</sup> (Knight field). In case (ii), the nuclear spin has a nonzero electric quadrupole moment, and therefore can interact directly with electric and strain fields via the local electric-field gradient<sup>59,63</sup>. Then, the direct interaction and the hyperfine-mediated interaction will compete. In both cases (i) and (ii), the results of our present work can serve as a starting point to evaluate the hyperfine-mediated contribution.

## VII. CONCLUSIONS

We have established the spin-strain and spin-stress interaction Hamiltonians for the NV ground state, and numerically determined the six independent parameters of this Hamiltonian using density functional theory. Focusing on the new Hamiltonian term  $H_{\varepsilon 1}$  identified in this work, we proposed an NV-based experimental setup where spin effects caused by a static mechanical deformation can be observed, and suggested coherent mechanical or electric spin control of the the magnetically allowed spin transitions. All qualitative considerations of this work should hold for the whole family of defects with  $C_{3v}$  symmetry and spin-1 electronic states.

## ACKNOWLEDGMENTS

We thank A. Auer, M. Barson, M. Doherty, A. Falk, J. Heremans, V. Ivády, J. Michl, S. Sangtawesin, D. Szaller, G. Thiering, and B. Zhou for helpful discussions. AP is supported by the National Research Development and Innovation Office of Hungary (NKFIH) Grants 105149 and 124723, and the ÚNKP-17-4-III New National Excellence Program of the Ministry of Human Capacities of Hungary. AG thanks for the support of the EU Commission in the DIADEMS project (Grant No. 611143) and NKFIH within the Quantum Technology National Excellence Program (Project No. 2017-1.2.1-NKP-2017-00001). VOS and GB are supported by the DFG within the collaborative research center SFB 767.

### Appendix A: Symmetry analysis of the spin-strain Hamiltonian

In this Appendix, we describe two derivations of the symmetry-allowed spin-strain Hamiltonian  $H_\varepsilon$  of Eq. (3). The first derivation is an elementary one, without reference to group representation theory, whereas the second one builds upon concepts of the latter. The two methods yield the same result Eq. (3).

#### 1. Elementary derivation

Our goal is to find the most general form of the Hamiltonian describing the interaction between a homogeneous strain and the ground-state spin (spin-1) of the NV. More precisely, we aim at finding the most general form of the interaction that is (i) allowed by the requirement of time reversal symmetry, (ii) allowed by the spatial symmetries ( $C_{3v}$ ) of the structure, (iii) linear in the elements of the strain tensor  $\varepsilon$ .

The interaction Hamiltonian should be quadratic in the components of the spin vector  $\mathbf{S} = (S_x, S_y, S_z)$ , as time reversal symmetry changes the sign of those, and the

interaction Hamiltonian should be invariant upon time reversal. Our  $\mathbf{S}$  is dimensionless, fulfilling  $S^2 = 2$ .

Therefore, our starting point is the Hamiltonian

$$H_\varepsilon = \sum_{\alpha, \beta, \gamma, \delta \in \{x, y, z\}} h_{\alpha\beta\gamma\delta} S_\alpha S_\beta \varepsilon_{\gamma\delta}, \quad (\text{A1})$$

where  $h$  is a four-dimensional matrix with real entries. Apparently,  $h$  has 81 independent elements; this will now be reduced, first without invoking any symmetries of the considered system.

To this end, we exploit the fact the 9-element set  $\{S_\alpha S_\beta | \alpha, \beta \in \{x, y, z\}\}$  is overcomplete (linearly dependent) in the six-dimensional vector space of  $3 \times 3$  Hermitian time-reversal invariant matrices. A six-element basis of that vector space is provided by, e.g.,  $(1, \frac{1}{2}\{S_x, S_y\}, \frac{1}{2}\{S_y, S_z\}, \frac{1}{2}\{S_z, S_x\}, S_z^2, S_x^2 - S_y^2) \equiv (\Sigma_0, \Sigma_1, \dots, \Sigma_5)$ . We will neglect the unit matrix  $\Sigma_0$  from now. Furthermore, we will refer to  $\Sigma$  as a map  $(S_x, S_y, S_z) \mapsto \Sigma(\mathbf{S}) := (\Sigma_1, \Sigma_2, \dots, \Sigma_5)$ .

A further simplification is allowed by the fact that the strain tensor is symmetric. Therefore it can be thought of as a six-dimensional column vector,  $\varepsilon = (\varepsilon_{xx}, \varepsilon_{yy}, \varepsilon_{zz}, \varepsilon_{yz}, \varepsilon_{zx}, \varepsilon_{xy})^T$ . We will consider  $\varepsilon$  as a function that maps the strain tensor to a six-dimensional vector,  $\varepsilon \mapsto \epsilon(\varepsilon)$ .

Using these simplifications, we can express the most general Hamiltonian as

$$H_\varepsilon = \sum_{n=1}^5 \sum_{v=1}^6 h_{nv} \Sigma_n \epsilon_v, \quad (\text{A2})$$

where  $h$  is a  $5 \times 6$  matrix with real entries, i.e., it is characterized by only 30 independent elements.

We will now further reduce this number using the spatial symmetry of the NV. Its symmetries are the isometries in the group  $C_{3v}$ . Those are generated by a 3-fold rotation around the  $z$  axis,  $\mathcal{R}$ , and the reflection on the  $xz$  plane,  $\mathcal{M}$ . These isometries are represented on a position vector by the  $3 \times 3$  matrices

$$R = \begin{pmatrix} \cos \frac{2\pi}{3} & -\sin \frac{2\pi}{3} & 0 \\ \sin \frac{2\pi}{3} & \cos \frac{2\pi}{3} & 0 \\ 0 & 0 & 1 \end{pmatrix}, \quad (\text{A3})$$

and

$$M = \begin{pmatrix} 1 & 0 & 0 \\ 0 & -1 & 0 \\ 0 & 0 & 1 \end{pmatrix}, \quad (\text{A4})$$

respectively.

A point isometry transforming the structure also transforms the associated physical quantities. For us, one of the relevant quantities is the strain tensor, which is transformed as  $\varepsilon \mapsto R\varepsilon R^{-1}$  and  $\varepsilon \mapsto M\varepsilon M^{-1}$ . The other relevant quantity is the spin vector, which transforms as a pseudovector (or axial vector). That is, the rotation is

represented on the spin as  $\mathbf{S} \mapsto R\mathbf{S}$ , but the reflection is represented as  $\mathbf{S} \mapsto M'\mathbf{S}$  with

$$M' = \begin{pmatrix} -1 & 0 & 0 \\ 0 & 1 & 0 \\ 0 & 0 & -1 \end{pmatrix}. \quad (\text{A5})$$

We require that the Hamiltonian is invariant against the transformations of the point group of the structure; formally that is written as

$$\sum_{n=1}^5 \sum_{v=1}^6 h_{nv} \Sigma_n(\mathbf{S}) \epsilon_v(\varepsilon) = \sum_{n=1}^5 \sum_{v=1}^6 h_{nv} \Sigma_n(R\mathbf{S}) \epsilon_v(R\varepsilon R^{-1}), \quad (\text{A6})$$

and

$$\sum_{n=1}^5 \sum_{v=1}^6 h_{nv} \Sigma_n(\mathbf{S}) \epsilon_v(\varepsilon) = \sum_{n=1}^5 \sum_{v=1}^6 h_{nv} \Sigma_n(M'\mathbf{S}) \epsilon_v(M\varepsilon M^{-1}), \quad (\text{A7})$$

Both of these equations form a homogeneous linear set of 30 equations, with the 30  $h_{nv}$  coupling-strength coefficients being the unknowns. Hence these equations establish linear relationships between the various  $h_{nv}$  coefficients, that is, they reduce the number of free parameters in the Hamiltonian.

These equations can be solved, e.g., symbolically using computer algebra. Inserting the solutions to  $H_\varepsilon$  yields our symmetry-allowed spin-strain interaction Hamiltonian of Eq. (3).

## 2. Derivation based on group representation theory

The  $C_{3v}$  symmetry group of the NV has three irreducible representations (irreps): the trivial 1D irrep  $A_1$ , the 1D irrep  $A_2$  and the 2D irrep  $E$ . The quadratic spin-component combinations that transform according to the trivial  $A_1$  irrep are

$$f_{A_1,1}^{(\text{spin})} = S_x^2 + S_y^2, \quad (\text{A8})$$

$$f_{A_1,2}^{(\text{spin})} = S_z^2. \quad (\text{A9})$$

Analogously, the linear strain-component combinations transforming as  $A_1$  are

$$f_{A_1,1}^{(\text{strain})} = \varepsilon_{xx} + \varepsilon_{yy}, \quad (\text{A10})$$

$$f_{A_1,2}^{(\text{strain})} = \varepsilon_{zz}. \quad (\text{A11})$$

We will refer to the number of these combinations as  $n(A_1) = 2$ . There are no such combinations transforming according to  $A_2$ , i.e.,  $n(A_2) = 0$ . The quadratic spin-component combinations forming 2D vectors, which transform according to the 2D irrep  $E$ , are

$$f_{E,1}^{(\text{spin})} = \begin{pmatrix} S_x^2 - S_y^2 \\ -\{S_x, S_y\} \end{pmatrix}, \quad (\text{A12})$$

$$f_{E,2}^{(\text{spin})} = \begin{pmatrix} \{S_x, S_z\} \\ \{S_y, S_z\} \end{pmatrix}. \quad (\text{A13})$$

Analogously, the linear strain-component combinations forming 2D vectors, which transform according to  $E$ , are

$$f_{E,1}^{(\text{strain})} = \begin{pmatrix} \varepsilon_{xx} - \varepsilon_{yy} \\ -2\varepsilon_{xy} \end{pmatrix}, \quad (\text{A14})$$

$$f_{E,2}^{(\text{strain})} = \begin{pmatrix} \varepsilon_{xz} \\ \varepsilon_{yz} \end{pmatrix}. \quad (\text{A15})$$

These imply  $n(E) = 2$ .

The symmetry-allowed spin-strain Hamiltonian is an arbitrary linear combination of the scalar products of the above-defined (1D and 2D) vectors that transform according to the same irrep. Formally, this is written in a compact fashion as follows:

$$H_\varepsilon = \sum_{\Gamma \in \text{irreps}} \sum_{\sigma, \tau=1}^{n(\Gamma)} c_{\Gamma\sigma\tau} \left( f_{\Gamma\sigma}^{(\text{spin})} \cdot f_{\Gamma\tau}^{(\text{strain})} \right). \quad (\text{A16})$$

Here, the quantities  $c_{\Gamma\sigma\tau}$  are independent real coefficients (coupling-strength parameters) that are not constrained by symmetry, and can be determined from microscopic models or experiments, as discussed in the main text. According to the counts of the previous paragraph, the sum in Eq. (A16) has 8 terms, and therefore there are 8 independent coupling-strength coefficients. However, since a uniform energy shift of the spin states in the Hamiltonian can be disregarded, and  $f_{A_1,1}^{(\text{spin})}$  and  $f_{A_1,1}^{(\text{strain})}$  do add up to a constant due to  $S_x^2 + S_y^2 + S_z^2 = 2$ , we can set  $c_{A_1,1,1} = c_{A_1,1,2} = 0$  without the loss of generality. This implies that there are six independent nonzero coupling-strength parameters.

Direct evaluation of the terms in Eq. (A16) and comparison with Eq. (3) allows to establish the relations between the coupling-strength coefficients:

$$c_{A_1,2,1} = h_{41}, \quad (\text{A17a})$$

$$c_{A_1,2,2} = h_{43}, \quad (\text{A17b})$$

$$c_{E,1,1} = \frac{1}{4} h_{15}, \quad (\text{A17c})$$

$$c_{E,1,2} = -\frac{1}{2} h_{16}, \quad (\text{A17d})$$

$$c_{E,2,1} = -\frac{1}{4} h_{25}, \quad (\text{A17e})$$

$$c_{E,2,2} = \frac{1}{2} h_{26}. \quad (\text{A17f})$$

## Appendix B: Computing spin-strain parameters with density functional theory

We determined the spin-strain coupling-strength parameters using numerical DFT calculations. We applied DFT for electronic structure calculation combined with geometry optimization, using the PBE functional<sup>66</sup> in the plane-wave-based Vienna Ab initio Simulation Package (VASP)<sup>67–70</sup>. The core electrons were treated in the

projector augmented-wave (PAW) formalism<sup>71</sup>. The calculations were performed with 600 eV plane wave cutoff energy. The model of the NV in bulk diamond was constructed using a 512-atom diamond simple cubic supercell within the  $\Gamma$ -point approximation. We use a negative sign convention for compressive strain. To model the structure subject to mechanical strain, described by the strain tensor  $\varepsilon$ , we deform the cubic supercell to a parallelepiped, whose edge vectors are obtained by transforming the undeformed edge vectors with the matrix  $1 + \varepsilon$  in the cubic reference frame, and allow the atomic positions to relax. For each strain configuration, the elements of the  $3 \times 3$  zero-field splitting matrix  $D$ , defining the ground-state spin Hamiltonian via  $H = \mathbf{S}^T \cdot D \cdot \mathbf{S}$ , were calculated using the VASP implementation by Martijn Marsman with the PAW formalism<sup>72</sup>.

We illustrate our methodology to obtain the six spin-strain coupling-strength coefficients with the example of  $h_{16}$ . To determine  $h_{16}$ , we deform the supercell using a strain tensor whose only nonvanishing element is  $\varepsilon_{yz}$ , and obtain the  $D$  matrix from the calculation. Due to Eq. (3), the chosen strain configuration implies that the Hamiltonian has the form

$$H = \frac{1}{2}\varepsilon_{yz}\mathbf{S}^T \cdot \begin{pmatrix} 0 & h_{16} & 0 \\ h_{16} & 0 & h_{26} \\ 0 & h_{26} & 0 \end{pmatrix} \mathbf{S}. \quad (\text{B1})$$

This, together with the above definition of the  $D$  matrix, yields

$$h_{16} = 2 \left. \frac{\partial D_{xy}}{\partial \varepsilon_{yz}} \right|_{\varepsilon=0}. \quad (\text{B2})$$

To be able to estimate the numerical error of our DFT calculations, we infer the derivative in Eq. (B2) using a sequence of calculations with 11 equidistant values of  $\varepsilon_{yz}$  between -0.01 and 0.01. The resulting  $D_{xy}(\varepsilon_{yz})$  data points are shown in Fig. 4. From a linear fit, shown as the solid line in Fig. 4, we infer the coupling-strength coefficient  $h_{16}$  via Eq. (B2) and its standard deviation.

Similar procedures can be applied to determine the remaining five coupling-strength parameters, and the results are shown in Table I, with the following remarks. (i) To obtain the value of  $h_{41}$  and its error in Table I, we calculated the corresponding results from the  $\varepsilon_{xx}$  dependence of the  $D$  matrix, as well as from its  $\varepsilon_{yy}$  dependence, and averaged these results. (ii) We used similar averaging in the case of  $h_{26}$  and  $h_{16}$ , which we calculated from from the  $\varepsilon_{xz}$  dependence, as well as from its  $\varepsilon_{yz}$  dependence (the latter is illustrated in Fig. 4). (iii) We determined the values for  $h_{25}$  and  $h_{15}$  from the  $\varepsilon_{xy}$  dependence. In Table I, we also present the spin-stress parameters ( $g_{41}$ , etc), which we determined from the DFT-based spin-strain parameters using the conversion procedure detailed in Appendix C.

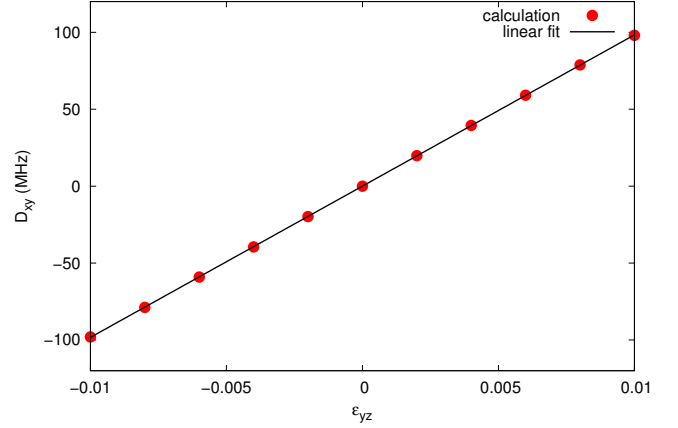


Figure 4. Strain dependence of the zero-field splitting matrix element  $D_{xy}$ . Data points show the DFT results for the matrix element  $D_{xy}$ , as a function of the strain component  $\varepsilon_{xy}$ , with all other strain components set to zero. Solid line shows a linear fit, with a slope of  $9832 \pm 9$  MHz/strain, allowing to obtain the coupling-strength parameter  $h_{16}$  via Eq. (B2).

### Appendix C: Converting spin-strain parameters to spin-stress parameters

To calculate the spin-stress coupling-strength parameters in Table I from the DFT-based spin-strain parameters, we start from the stiffness tensor  $C$  of bulk diamond, and take the following values<sup>73</sup> for its elements in the cubic reference frame:  $C_{11} = 1076$  GPa,  $C_{12} = 125$  GPa,  $C_{44} = 576$  GPa. First, we transform the stiffness tensor to the NV frame; we denote the resulting  $6 \times 6$  stiffness matrix in the Voigt notation as  $C$ . To convert our spin-strain Hamiltonian Eq. (3) to spin-stress Hamiltonian, we express the strain components in Eq. (3) using stress components via  $\varepsilon = C^{-1}\sigma$ , where  $\varepsilon = (\varepsilon_{xx}, \varepsilon_{yy}, \varepsilon_{zz}, 2\varepsilon_{yz}, 2\varepsilon_{zx}, 2\varepsilon_{xy})$  and  $\sigma = (\sigma_{xx}, \sigma_{yy}, \sigma_{zz}, \sigma_{yz}, \sigma_{zx}, \sigma_{xy})$  are now also in Voigt notation; note the factor of two in front of the off-diagonal strain components.

The inverted stiffness tensor in the NV frame reads

$$C^{-1} = \begin{pmatrix} C_{11}^{-1} & C_{12}^{-1} & C_{13}^{-1} & 0 & C_{15}^{-1} & 0 \\ C_{12}^{-1} & C_{11}^{-1} & C_{13}^{-1} & 0 & -C_{15}^{-1} & 0 \\ C_{13}^{-1} & C_{13}^{-1} & C_{33}^{-1} & 0 & 0 & 0 \\ 0 & 0 & 0 & C_{44}^{-1} & 0 & C_{46}^{-1} \\ C_{15}^{-1} & -C_{15}^{-1} & 0 & 0 & C_{44}^{-1} & 0 \\ 0 & 0 & 0 & C_{46}^{-1} & 0 & C_{66}^{-1} \end{pmatrix}, \quad (\text{C1})$$

yielding the following following expressions for the spin-

stress parameters:

$$g_{41} = h_{41} (C_{11}^{-1} + C_{12}^{-1}) + h_{43} C_{13}^{-1} \quad (\text{C2a})$$

$$g_{43} = 2h_{41} C_{13}^{-1} + h_{43} C_{33}^{-1} \quad (\text{C2b})$$

$$g_{26} = h_{26} \frac{1}{2} C_{44}^{-1} - h_{25} C_{15}^{-1} \quad (\text{C2c})$$

$$g_{25} = h_{25} (C_{11}^{-1} - C_{12}^{-1}) - h_{26} C_{15}^{-1} \quad (\text{C2d})$$

$$g_{16} = h_{16} \frac{1}{2} C_{44}^{-1} - h_{15} C_{15}^{-1} \quad (\text{C2e})$$

$$g_{15} = h_{15} (C_{11}^{-1} - C_{12}^{-1}) - h_{16} C_{15}^{-1} \quad (\text{C2f})$$

These relations, together with the numerical values of the inverse stiffness matrix elements,

$$\begin{aligned} C_{11}^{-1} &= 86 \cdot 10^{-5} \text{ 1/GPa}, & C_{33}^{-1} &= 83 \cdot 10^{-5} \text{ 1/GPa}, \\ C_{44}^{-1} &= 198 \cdot 10^{-5} \text{ 1/GPa}, & C_{66}^{-1} &= 186 \cdot 10^{-5} \text{ 1/GPa}, \\ C_{12}^{-1} &= -7 \cdot 10^{-5} \text{ 1/GPa}, & C_{13}^{-1} &= -4 \cdot 10^{-5} \text{ 1/GPa}, \\ C_{15}^{-1} &= 9 \cdot 10^{-5} \text{ 1/GPa}, & C_{46}^{-1} &= -17 \cdot 10^{-5} \text{ 1/GPa}, \end{aligned}$$

are used to obtain the  $g_{41}$ , etc values in Table I.

- 
- <sup>1</sup> L. du Preez, Ph.D. thesis, University of Witwatersrand (1965).
- <sup>2</sup> G. Davies and M. F. Hamer, Proc. R. Soc. London Ser. A **348**, 285 (1976).
- <sup>3</sup> J. H. N. Loubser and J. P. van Wyk, in *Diamond Research (London)* (Industrial Diamond information Bureau, London, 1977) pp. 11–15.
- <sup>4</sup> J. P. Goss, R. Jones, S. J. Breuer, P. R. Briddon, and S. Öberg, Phys. Rev. Lett. **77**, 3041 (1996).
- <sup>5</sup> N. B. Manson, J. P. Harrison, and M. J. Sellars, Physical Review B **74**, 104303 (2006).
- <sup>6</sup> A. Gali, M. Fyta, and E. Kaxiras, Phys. Rev. B **77**, 155206 (2008).
- <sup>7</sup> F. Jelezko, T. Gaebel, I. Popa, A. Gruber, and J. Wrachtrup, Phys. Rev. Lett. **92**, 076401 (2004).
- <sup>8</sup> A. Gruber, A. Dräbenstedt, C. Tietz, L. Fleury, J. Wrachtrup, and C. von Borczyskowski, Science **276**, 2012 (1997).
- <sup>9</sup> G. Balasubramanian, P. Neumann, D. Twitchen, M. Markham, R. Kolesov, N. Mizuochi, J. Isoya, J. Achard, J. Beck, J. Tjessler, V. Jacques, P. R. Hemmer, F. Jelezko, and J. Wrachtrup, Nature Mater. **8**, 383 (2009).
- <sup>10</sup> H. Bernien, B. Hensen, W. Pfaff, G. Koolstra, M. S. Blok, L. Robledo, T. H. Taminiau, M. Markham, D. J. Twitchen, L. Childress, and R. Hanson, Nature **497**, 86 (2013).
- <sup>11</sup> B. Hensen, H. Bernien, A. E. Drau, A. Reiserer, N. Kalb, M. S. Blok, J. Ruitenber, R. F. L. Vermeulen, R. N. Schouten, C. Abelln, W. Amaya, V. Pruneri, M. W. Mitchell, M. Markham, D. J. Twitchen, D. Elkouss, S. Wehner, T. H. Taminiau, and R. Hanson, Nature **526**, 682 (2015).
- <sup>12</sup> N. Kalb, A. A. Reiserer, P. C. Humphreys, J. J. W. Bakermans, S. J. Kamerling, N. H. Nickerson, S. C. Benjamin, D. J. Twitchen, M. Markham, and R. Hanson, Science **356**, 928 (2017).
- <sup>13</sup> G. Balasubramanian, I. Y. Chan, R. Kolesov, M. Al-Hmoud, J. Tisler, C. Shin, C. Kim, A. Wojcik, P. R. Hemmer, A. Krueger, T. Hanke, A. Leitenstorfer, R. Bratschitsch, F. Jelezko, and J. Wrachtrup, Nature **455**, 648 (2008).
- <sup>14</sup> J. R. Maze, P. L. Stanwix, J. S. Hodges, S. Hong, J. M. Taylor, P. Cappellaro, L. Jiang, M. V. G. Dutt, E. Togan, A. S. Zibrov, A. Yacoby, R. L. Walsworth, and M. D. Lukin, Nature **455**, 644 (2008).
- <sup>15</sup> F. Dolde, H. Fedder, M. W. Doherty, T. Nbauer, F. Rempp, G. Balasubramanian, T. Wolf, F. Reinhard, L. C. L. Hollenberg, F. Jelezko, and J. Wrachtrup, Nat Phys **7**, 459 (2011).
- <sup>16</sup> D. M. Toyli, C. F. d. l. Casas, D. J. Christle, V. V. Dobrovitski, and D. D. Awschalom, PNAS **110**, 8417 (2013).
- <sup>17</sup> P. Neumann, I. Jakobi, F. Dolde, C. Burk, R. Reuter, G. Waldherr, J. Honert, T. Wolf, A. Brunner, J. H. Shim, D. Suter, H. Sumiya, J. Isoya, and J. Wrachtrup, Nano Lett. **13**, 2738 (2013).
- <sup>18</sup> G. Kucsko, P. C. Maurer, N. Y. Yao, M. Kubo, H. J. Noh, P. K. Lo, H. Park, and M. D. Lukin, Nature **500**, 54 (2013).
- <sup>19</sup> J. Teissier, A. Barfuss, P. Appel, E. Neu, and P. Maletinsky, Phys. Rev. Lett. **113**, 020503 (2014).
- <sup>20</sup> A. Barfuss, J. Teissier, E. Neu, A. Nunnenkamp, and P. Maletinsky, Nat Phys **11**, 820 (2015).
- <sup>21</sup> P. Ovarthaiyapong, K. W. Lee, B. A. Myers, and A. C. B. Jayich, Nat. Commun. **5** (2014).
- <sup>22</sup> J. Cramer, N. Kalb, M. A. Rol, B. Hensen, M. S. Blok, M. Markham, D. J. Twitchen, R. Hanson, and T. H. Taminiau, Nat. Comm. **7**, 11526 EP (2016).
- <sup>23</sup> G. Waldherr, Y. Wang, S. Zaiser, M. Jamali, T. Schulte-Herbruggen, H. Abe, T. Ohshima, J. Isoya, J. F. Du, P. Neumann, and J. Wrachtrup, Nature **506**, 204 (2014).
- <sup>24</sup> T. H. Taminiau, J. Cramer, T. van der Sar, V. V. Dobrovitski, and R. Hanson, Nat Nano **9**, 171 (2014).
- <sup>25</sup> J. R. Maze, A. Gali, E. Togan, Y. Chu, A. Trifonov, E. Kaxiras, and M. D. Lukin, New Journal of Physics **13**, 025025 (2011).
- <sup>26</sup> M. W. Doherty, N. B. Manson, P. Delaney, and L. C. L. Hollenberg, New Journal of Physics **13**, 025019 (2011).
- <sup>27</sup> M. W. Doherty, F. Dolde, H. Fedder, F. Jelezko, J. Wrachtrup, N. B. Manson, and L. C. L. Hollenberg, Phys. Rev. B **85**, 205203 (2012).
- <sup>28</sup> M. W. Doherty, N. B. Manson, P. Delaney, F. Jelezko, J. Wrachtrup, and L. C. Hollenberg, Phys. Rep. **528**, 1 (2013).
- <sup>29</sup> J. Cai, F. Jelezko, and M. B. Plenio, Nature Communications **5**, 4065 EP (2014).
- <sup>30</sup> E. R. MacQuarrie, T. A. Gosavi, A. M. Moehle, N. R. Jungwirth, S. A. Bhave, and G. D. Fuchs, Optica **2**, 233 (2015).
- <sup>31</sup> E. R. MacQuarrie, T. A. Gosavi, N. R. Jungwirth, S. A. Bhave, and G. D. Fuchs, Phys. Rev. Lett. **111**, 227602 (2013).
- <sup>32</sup> E. R. MacQuarrie, M. Otten, S. K. Gray, and G. D. Fuchs, Nat. Comm. **8**, 14358 (2017).
- <sup>33</sup> E. R. MacQuarrie, T. A. Gosavi, S. A. Bhave, and G. D. Fuchs, Phys. Rev. B **92**, 224419 (2015).

- <sup>34</sup> M. S. J. Barson, P. Peddibhotla, P. Ovarthaiyapong, K. Ganesan, R. L. Taylor, M. Gebert, Z. Mielens, B. Koslowski, D. A. Simpson, L. P. McGuinness, J. McCallum, S. Praver, S. Onoda, T. Ohshima, A. C. Bleszynski Jayich, F. Jelezko, N. B. Manson, and M. W. Doherty, *Nano Letters* **17**, 1496 (2017), pMID: 28146361, <http://dx.doi.org/10.1021/acs.nanolett.6b04544>.
- <sup>35</sup> D. A. Golter, T. Oo, M. Amezcua, K. A. Stewart, and H. Wang, *Phys. Rev. Lett.* **116**, 143602 (2016).
- <sup>36</sup> D. A. Golter, T. Oo, M. Amezcua, I. Lekavicius, K. A. Stewart, and H. Wang, *Phys. Rev. X* **6**, 041060 (2016).
- <sup>37</sup> S. Meesala, Y.-I. Sohn, H. A. Atikian, S. Kim, M. J. Burek, J. T. Choy, and M. Lončar, *Phys. Rev. Applied* **5**, 034010 (2016).
- <sup>38</sup> E. van Oort and M. Glasbeek, *Chemical Physics Letters* **168**, 529 (1990).
- <sup>39</sup> M. Matsumoto, K. Chimata, and M. Koga, *Journal of the Physical Society of Japan* **86**, 034704 (2017), <http://dx.doi.org/10.7566/JPSJ.86.034704>.
- <sup>40</sup> Y. Kato, R. C. Myers, A. C. Gossard, and D. D. Awschalom, *Nature* **427**, 50 (2004).
- <sup>41</sup> K. C. Nowack, F. H. L. Koppens, Y. V. Nazarov, and L. M. K. Vandersypen, *Science* **318**, 1430 (2007), <http://science.sciencemag.org/content/318/5855/1430.full.pdf>.
- <sup>42</sup> V. N. Golovach, M. Borhani, and D. Loss, *Phys. Rev. B* **74**, 165319 (2006).
- <sup>43</sup> P. V. Klimov, A. L. Falk, B. B. Buckley, and D. D. Awschalom, *Phys. Rev. Lett.* **112**, 087601 (2014).
- <sup>44</sup> A. Norambuena, E. Munoz, H. T. Dinani, A. Jarmola, P. Maletinsky, D. Budker, and J. R. Maze.
- <sup>45</sup> Note that with respect to the values quoted in Ref. 34, the values in the fourth column of Table II have an inverted sign, because of the different sign convention for the stress tensor: we assign a negative stress to compression.
- <sup>46</sup> D. A. Broadway, J. D. A. Wood, L. T. Hall, A. Stacey, M. Markham, D. A. Simpson, J.-P. Tetienne, and L. C. L. Hollenberg, *Phys. Rev. Applied* **6**, 064001 (2016).
- <sup>47</sup> V. Jacques, P. Neumann, J. Beck, M. Markham, D. Twitchen, J. Meijer, F. Kaiser, G. Balasubramanian, F. Jelezko, and J. Wrachtrup, *Phys. Rev. Lett.* **102**, 057403 (2009).
- <sup>48</sup> V. Ivády, P. V. Klimov, K. C. Miao, A. L. Falk, D. J. Christle, K. Szász, I. A. Abrikosov, D. D. Awschalom, and A. Gali, *Phys. Rev. Lett.* **117**, 220503 (2016).
- <sup>49</sup> S. Felton, A. M. Edmonds, M. E. Newton, P. M. Martineau, D. Fisher, D. J. Twitchen, and J. M. Baker, *Phys. Rev. B* **79**, 075203 (2009).
- <sup>50</sup> F. Jelezko, T. Gaebel, I. Popa, M. Domhan, A. Gruber, and J. Wrachtrup, *Phys. Rev. Lett.* **93**, 130501 (2004).
- <sup>51</sup> G. D. Fuchs, V. V. Dobrovitski, D. M. Toyli, F. J. Heremans, and D. D. Awschalom, *Science* **326**, 1520 (2009), <http://www.sciencemag.org/content/326/5959/1520.full.pdf>.
- <sup>52</sup> M. J. A. Schuetz, E. M. Kessler, G. Giedke, L. M. K. Vandersypen, M. D. Lukin, and J. I. Cirac, *Phys. Rev. X* **5**, 031031 (2015).
- <sup>53</sup> A. Crippa *et al.*, “Electrical spin driving by g-matrix modulation in spin-orbit qubits,” ArXiv:1710.08690 (unpublished).
- <sup>54</sup> G. D. Fuchs, G. Burkard, P. V. Klimov, and D. D. Awschalom, *Nature Phys.* **7**, 789 (2011).
- <sup>55</sup> L. Childress, M. V. Gurudev Dutt, J. M. Taylor, A. S. Zibrov, F. Jelezko, J. Wrachtrup, P. R. Hemmer, and M. D. Lukin, *Science* **314**, 281 (2006), <http://science.sciencemag.org/content/314/5797/281.full.pdf>.
- <sup>56</sup> L. Robledo, L. Childress, H. Bernien, B. Hensen, P. F. A. Alkemade, and R. Hanson, *Nature* **477**, 574 (2011).
- <sup>57</sup> M. Ogura and H. Akai, *Applied Physics Letters* **91**, 253118 (2007), <http://dx.doi.org/10.1063/1.2825423>.
- <sup>58</sup> S. Thiele, F. Balestro, R. Ballou, S. Klyatskaya, M. Ruben, and W. Wernsdorfer, *Science* **344**, 1135 (2014), <http://science.sciencemag.org/content/344/6188/1135.full.pdf>.
- <sup>59</sup> A. J. Sigillito, A. M. Tyryshkin, T. Schenkel, A. A. Houck, and S. A. Lyon, *Nat Nano* **12**, 958 (2017).
- <sup>60</sup> G. Tosi, F. A. Mohiyaddin, S. Tenberg, A. Laucht, and A. Morello, “Robust electric dipole transition at microwave frequencies for nuclear spin qubits in silicon,” ArXiv:1706.08095 (unpublished).
- <sup>61</sup> P. Boross, G. Széchenyi, and A. Pályi, “Hyperfine-assisted fast electric control of dopant nuclear spins in semiconductors,” ArXiv:1707.00581 (unpublished).
- <sup>62</sup> J. Mansir, P. Conti, Z. Zeng, J. J. Pla, P. Bertet, B. Sklenard, Y.-M. Niquet, and J. J. Morton, “Linear hyperfine tuning of donor spins in silicon using hydrostatic strain,” ArXiv:1710.00723 (unpublished).
- <sup>63</sup> C. P. Slichter, *Principles of Magnetic Resonance* (Harper & Row, New York, 1963).
- <sup>64</sup> S. Sangtawesin, C. A. McLellan, B. A. Myers, A. C. B. Jayich, D. D. Awschalom, and J. R. Petta, *New Journal of Physics* **18**, 083016 (2016).
- <sup>65</sup> M. Chen, M. Hirose, and P. Cappellaro, *Phys. Rev. B* **92**, 020101 (2015).
- <sup>66</sup> J. P. Perdew, K. Burke, and M. Ernzerhof, *Phys. Rev. Lett.* **77**, 3865 (1996).
- <sup>67</sup> G. Kresse and J. Hafner, *Phys. Rev. B* **47**, 558 (1993).
- <sup>68</sup> G. Kresse and J. Furthmüller, *Phys. Rev. B* **54**, 11169 (1996).
- <sup>69</sup> G. Kresse and J. Furthmüller, *Computational Materials Science* **6**, 15 (1996).
- <sup>70</sup> J. Paier, M. Marsman, K. Hummer, G. Kresse, I. C. Gerber, and J. G. Ángyán, *The Journal of Chemical Physics* **124**, 154709 (2006).
- <sup>71</sup> P. E. Blöchl, *Phys. Rev. B* **50**, 17953 (1994).
- <sup>72</sup> Z. Bodrog and A. Gali, *Journal of Physics: Condensed Matter* **26**, 015305 (2014).
- <sup>73</sup> E. Kaxiras, *Atomic and Electronic Structure of Solids* (Cambridge University Press, 2003).